ACS APPLIED MATERIALS & INTERFACES

Research Article

www.acsami.org

# Preparation of Hollow Core/Shell Microspheres of Hematite and Its Adsorption Ability for Samarium

Sheng-Hui Yu,[†] Qi-Zhi Yao,[‡] Gen-Tao Zhou,[†,*] and Sheng-Quan Fu[§]

[†]CAS Key Laboratory of Crust-Mantle Materials and Environments, School of Earth and Space Sciences, [‡]School of Chemistry and Materials Science, and [§]Hefei National Laboratory for Physical Sciences at Microscale, University of Science and Technology of China, Hefei 230026, P. R. China

**ABSTRACT:** Hollow core/shell hematite microspheres with diameter of ca. 1−2 μm have been successfully achieved by calcining the precursor composite microspheres of pyrite and polyvinylpyrrolidone (PVP) in air. The synthesized products were characterized by a wide range of techniques including powder X-ray diffraction (XRD), field-emission scanning electron microscopy (FESEM), energy-dispersive X-ray spectroscopy (EDX), transmission electron microscopy (TEM), high-resolution TEM (HRTEM), thermogravimetric analysis (TGA) and differential scanning calorimetry (DSC), and Brunauer−Emmett−Teller (BET) gas sorptometry. Temperature- and time-dependent experiments unveil that the precursor pyrite-PVP composite microspheres finally transform into hollow core/shell hematite microspheres in air through a multistep process including the oxidation and sulfation of pyrite, combustion of PVP occluded in the precursor, desulfation, aggregation, and fusion of nanosized hematite as well as mass transportation from the interior to the exterior of the microspheres. The formation of the hollow core/shell microspheres dominantly depends on the calcination temperature under current experimental conditions, and the aggregation of hematite nanocrystals and the core shrinking during the oxidation of pyrite are responsible for the formation of the hollow structures. Moreover, the adsorption ability of the hematite for Sm(III) was also tested. The results exhibit that the hematite microspheres have good adsorption activity for trivalent samarium, and that its adsorption capacity strongly depends on the pH of the solution, and the maximum adsorption capacity for Sm(III) is 14.48 mg/g at neutral pH. As samarium is a typical member of the lanthanide series, our results suggest that the hollow hematite microspheres have potential application in removal of rare earth elements (REEs) entering the water environment.

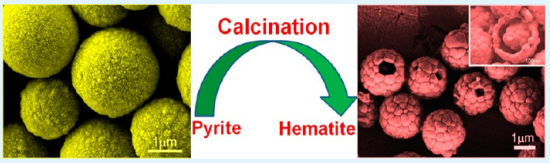


**KEYWORDS:** *hematite, core/shell structure, pyrite, adsorption, samarium*

## INTRODUCTION

Hematite ($\alpha$-$Fe_2O_3$), the most thermodynamically stable iron oxide with n-type semiconducting properties under ambient conditions, is widespread in nature and readily synthesized in the laboratory.[1] Because of its fascinating and peculiar physicochemical properties, low processing cost, high stability, and environmental friendliness, hematite has attracted great attention from researchers in various fields and has been applied as pigments,[1] catalysts,[2] gas sensors,[3,4] drug delivery,[5] magnetic devices,[6] electrode materials in lithium-ion batteries,[7,8] adsorbents for treating water pollution,[9−12] and the raw materials for preparation of $\gamma$-$Fe_2O_3$. In past decades, researchers have successfully prepared numerous nano- and micrometer hematite with controlled morphologies, such as 0D nanoparticles;[13] 1D nanowires, nanorods, or nanotubes;[14−16] 2D plates or sheets;[17,18] and 3D microspheres and urchine- or flower-like structures,[19−21] as well as hybrid composites.[22−24] Among these different morphologies, hematite with complex hierarchical structures is more attractive to researchers,[25,26] because of its properties of low density, high surface area, and excellent surface permeability compared with ordinary hematite. Up to now, the most extensively used methodologies in the laboratory to prepare hematite with controlled morphology or/and size are sol−gel method,[27] hydrothermal or solvothermal technique,[28,29] and template-directed synthetic route.[30] In recent years, many new synthetic methods to prepare hematite with special 3D nanostructures have also been emerging. For example, Wan's group synthesized a novel flowerlike iron oxide nanostructures by thermal decomposition of precursors, which were obtained by an ethylene glycol (EG)-mediated self-assembly process.[31] Using a two-step synthesis method, Cao et al. successfully prepared $\alpha$-$Fe_2O_3$ hollow spheres by thermal decomposition of a precursor which was synthesized by a microwave-assisted solvothermal method, using $FeCl_3 \cdot 6H_2O$, NaOH, and sodium dodecylbenzenesulfonate in the solvent ethylene glycol.[32] Cheng et al. fabricated durian-like hematite hollow spheres by liquid−liquid interface-assisted solvothermal method.[33] However, seeking facile, economic, and green methods to prepare well-crystallized hematite with controllable surface texture, complex architecture, and excellent properties is still a challenge and pursuit to researchers in the field of materials science.

Pyrite ($FeS_2$) is a naturally occurring material that can be found in concentrated form in nature and also as impurities in

Received: April 9, 2014
Accepted: June 3, 2014
Published: June 3, 2014

  

coal and many other minerals. Because of its potential as a useful material for solar-energy applications,[34−36] as the cathode for high-energy-density batteries,[37] and as depolarizer anode for hydrogen production,[38] pyrite has also received growing attention in recent years. The synthesis of pyrite with different shapes and sizes has been reported by many researchers.[39−41] The transformation of pyrite in an oxygen-containing atmosphere is a complicated process, and may proceed by different mechanisms under different conditions. Parameters such as temperature, particle size, flow condition and properties of the surrounding atmosphere can all affect final phases.[42] There is a general agreement that the finally oxidized product of pyrite in air is hematite.[43] This may provide a new route to prepare hematite.

In this paper, hollow core/shell hematite microspheres with hierarchical structure were prepared by calcining precursor composite microspheres of pyrite and polyvinylpyrrolidone (PVP). The precursor microspheres were synthesized by a facile microwave-assisted reflux method, as previously reported by our group,[44] using ferrous sulfate, sulfur powder, polyvinylpyrrolidone (PVP) and ethylene glycol (EG) as initial materials. Moreover, the adsorption ability of the hollow core/shell hematite microspheres for samarium(III) was also evaluated. To the best of our knowledge, the synthetic route and special architecture of hematite have not been reported so far.

## EXPERIMENTAL SECTION

All chemical reagents were of analytical grade and used as received without any further purification. The microwave reactor used for the preparation of the precursor is a microwave-reflux synthesis system (WBFY-201, Yuhua, Gongyi, China), with cycle period of 22 s, output power of 800 W, working frequency of $2.45 \times 10^9$ Hz. The microwave reactor can operate at 10, 30, 50, 80, and 100% full power by changing the on/off duration of the microwave irradiation on cycle model. A programmed furnace (KSL-1100, Kmt, China) was used for the calcination of the synthesized precursor.

In a typical synthetic procedure, the composite microspheres of pyrite and polyvinylpyrrolidone (PVP) were first synthesized, briefly, 0.556 g of $FeSO_4 \cdot 7H_2O$ and 0.6 g of PVP-K30 were dissolved in 20 mL of ethylene glycol in a 100 mL round-bottomed flask. Then 0.128 g of S powder was dispersed in the solution by ultrasonication for a few minutes. The round-bottomed flask was equipped on the microwave reactor for reaction of 30 min under nitrogen flow at 80% of the full power, and a black precipitate was obtained. The dried black precipitate was then calcined in air at 900 °C for 10 min, with a heating rate of 5 °C $min^{-1}$ and cooled to room temperature naturally. Finally, a red powder was obtained and collected for further characterizations.

Several analytical techniques were used to characterize the synthesized products. Powder X-ray diffraction (XRD) patterns of the synthesized samples were recorded with a Japan Map XHF X-ray diffractometer equipped with graphite-monochromatized Cu K$\alpha$ irradiation ($\lambda$ = 0.154056 nm), employing a scanning rate of 0.02° $s^{-1}$ in the 2$\theta$ range of 20−80°. Microstructures of the precursor and calcined products were observed by JEOL JSM-2010 field-emission scanning electron microscopy (FESEM). Energy-dispersive X-ray spectroscopy (EDX) analyses were obtained with an EDAX detector installed on the same FESEM. The images of transmission electron microscopy (TEM) and high-resolution transmission electron microscopy (HRTEM) were obtained on a JEM-2010 microscope operated at an acceleration voltage of 200 kV. Nitrogen adsorption−desorption isotherms at the temperature of liquid nitrogen were measured with a Micromeritics Coulter (USA) instrument. Thermogravimetric analysis (TGA) and differential scanning calorimetry (DSC) were carried out on SDT Q600 thermal analyzer with a heating rate of 10 °C $min^{-1}$ in air.

The stock solution of samarium(III) was prepared by dissolving samarium oxide ($Sm_2O_3$) in diluted hydrochloric acid, 300 mg/L ($2 \times 10^{-3}$ mol $L^{-1}$), and diluted to the concentration of 15 mg/L ($10^{-4}$ mol $L^{-1}$). All batch experiments were carried out by mixing 0.030 g of the hematite with 30 mL of aqueous solution of samarium. The experiments were conducted in triplicate, and averaged values were reported. The effect of pH on the adsorption activity of the hierarchical nanostructured hematite was investigated, and the pH varied from 2 to 8. The pH of the solution was adjusted with HCl and/or NaOH and recorded with a pH meter. In addition, the effect of the contact time on the adsorption activity and adsorption capacity of the hematite microspheres were also investigated at pH 7.0 ± 0.1. The supernatant of the suspension was collected by centrifugation at 10000 rpm for 5 min, and then the concentration of samarium was analyzed using inductively coupled plasma atomic emission spectroscopy (ICP-AES, optima 7300 DV). The amount of samarium adsorbed at time $t$, $q_t$ (mg/g), uptake percentage $U$ %, and the amount of samarium adsorbed at equilibrium, $q_e$ (mg/g), were calculated according to following equations, respectively:

$$q_t = \frac{(C_o - C_t)V}{W}$$

$$U\% = \frac{(C_o - C_t)100\%}{C_o}$$

$$q_e = \frac{(C_o - C_e)V}{W}$$

where $C_o$ (mg/L), $C_t$ (mg/L), and $C_e$ are the liquid phase concentration of the samarium at initial, any time t and equilibrium, respectively. $V$ is the volume of the solution (mL) and $W$ is the mass of the hematite added (mg).

## RESULTS AND DISCUSSION

A typical XRD pattern and SEM image of the precursor prepared by microwave-assisted reflux method are shown in

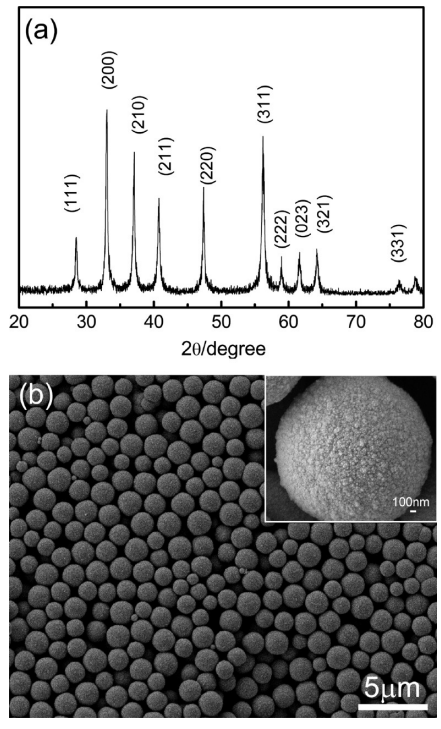


**Figure 1.** (a) Typical XRD pattern and (b) SEM image of precursor microspherolites; inset in panel b: the close-up image of a single precursor microsphere.

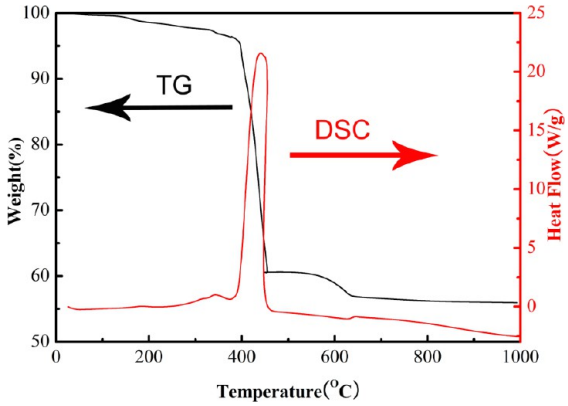


**Figure 2.** TG/DSC curves of the precursor microspheres.

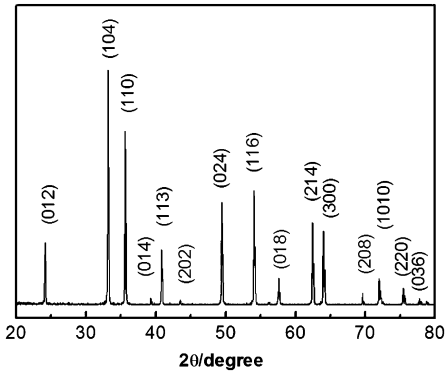


**Figure 3.** Typical XRD pattern of the precursor calcined at 900 °C for 10 min.

Figure 1. One can find from Figure 1a that the XRD pattern is the same as the reported results,[44] and all of the diffraction peaks can be indexed to a cubic lattice of pure pyrite $FeS_2$ (JCPDS card No.89−3057; space group $Pa\bar{3}$), indicating that a pure phase pyrite is obtained. The SEM image of the pyrite in Figure 1b shows that the pyrite exhibits a spherical morphology with an average diameter of about 2 $\mu$m, and further magnified SEM image (inset in Figure 1b) reveals that the microspheres are composed of small nanocrystallites ∼20−30 nm in size, endowing with the spherolite-like textures, which is the same as the reported results as well.[44] Both the XRD pattern and SEM images of the precursor demonstrate that the preparation for the pyrite precursor can be easily achieved.

Thermal behavior of the precursor was examined by TG and DSC techniques in a flowing air atmosphere. The typical TG and DSC curves of the precursor are shown in Figure 2. An obvious two weight loss stages can be observed on the TG curve. Nevertheless, the main feature of the DSC trace is a large and broad exothermic peak, which occurs at temperatures between 390 and 450 °C and corresponds to the first significant weight loss stage. The large and broad exothermic peak and the corresponding significant weight loss may indicate that the multistep complex reactions occur in this stage, including the oxidation and decomposition of pyrite, the formation of iron sulfates and the combustion of PVP possibly anchoring to the pyrite microspheres. The detailed discussions would be depicted later. Moreover, there is an arrest (the second weight loss stage) from 450 to 640 °C on the TG curve. According to several previous investigations,[43,45−48] this arrest can be ascribable to the decomposition of iron sulfates ($Fe_2(SO_4)_3$ and $FeSO_4$) formed in the first weight loss stage. Summarizing, the TG analysis reveals a ∼44% of total weight loss from room temperature to 900 °C, and hence the yield of hematite is 56%. On the basis of the stoichiometry of the complete oxidation of $FeS_2$ to $Fe_2O_3$, it is not difficult to be estimated that pure $FeS_2$ accounts for ∼84% in the precursor microspheres. Therefore, PVP occluded in the precursor pyrite microspheres is about 16%, indicating that the precursor synthesized by this method is an organic−inorganic composite.

Figure 3 presents a typical XRD pattern of the precursor pyrite-PVP composite microspheres calcined at 900 °C for 10 min. All diffraction peaks can be easily indexed to the pure rhombohedral phase of $\alpha$-$Fe_2O_3$ with calculated lattice parameters $a$ = 5.035 Å and $c$ = 13.746 Å, which are in good agreement with the literature values (JCPDS 33−0664; space group $R\bar{3}c$). The narrow sharp peaks of the XRD pattern indicate that the $\alpha$-$Fe_2O_3$ is well-crystallized. No characteristic peaks belonging to pyrite, other sulfides, $Fe_3O_4$ or $\gamma$-$Fe_2O_3$ can be found, suggesting that a facile calcining process can lead to the formation of phase purity hematite. Furthermore, EDX was also utilized to identify the chemical element composition of the product. As shown in Figure 4a inset, the calcined sample mainly contains Fe and O elements, in addition to the Au peaks which come from sputtering, further confirming the formation of iron oxides.

The nature of morphology and architecture of the hematite microspheres was investigated by SEM and TEM techniques. Typical SEM and TEM micrographs of the calcined product are shown in Figure 4a-c. The panoramic SEM image in Figure 4a provides a representative overview of the sample after 900 °C calcination treatment for 10 min. It can be seen that the calcined sample still exhibits uniform spherical morphology, and the average diameter is about 2 $\mu$m, similar to the size of precursor microspherolites, indicating that calcining process can easily lead to the intact formation of the spherical structures. Therefore, the precursor microsphere itself may also act as a hard template during the formation of the hollow hematite microsphere. Further magnified SEM image (Figure 4c) reveals that the surface texture of the microspheres is not smooth, and is almost composed of quasi-pentagon and hexagon patches, forming football-like architectures, as highlighted in Figure 4c. Moreover, some broken microspheres shown in Figure 4b indicate that the calcined product may not be a solid architecture, but a hollow structure. The close-up image of a single broken sphere (Figure 4c inset) shows that the $\alpha$-$Fe_2O_3$ microspheres have a core/shell structure with a solid core inside the hollow spheres (as indicated by arrows in Figure 4c inset), which are also hierarchically structured by submicrometer particles. The TEM image of a random spherolite in Figure 4e further confirms that the hematite microspheres are of a hollow core/shell structure, the distinct contrasts between the black part and the light part of the spherolite unveil that the microspheres have the circular empty space in between the core and shell. In short, a series of SEM and TEM analyses demonstrate that the product obtained by thermal decomposition of the pyrite-PVP microspherolites is hierarchically hollow core/shell microspheres. Moreover, in order to get insight into the microstructure of the building units (the quasi-pentagon and hexagon patches), the hematite microspheres were carefully grinded. Figure 4f shows a typical HRTEM image of a detached patch. The well-resolved lattice fringes ascertain that the building units are well crystallized. The fringe spacing is 0.160 nm, which occurs well with the

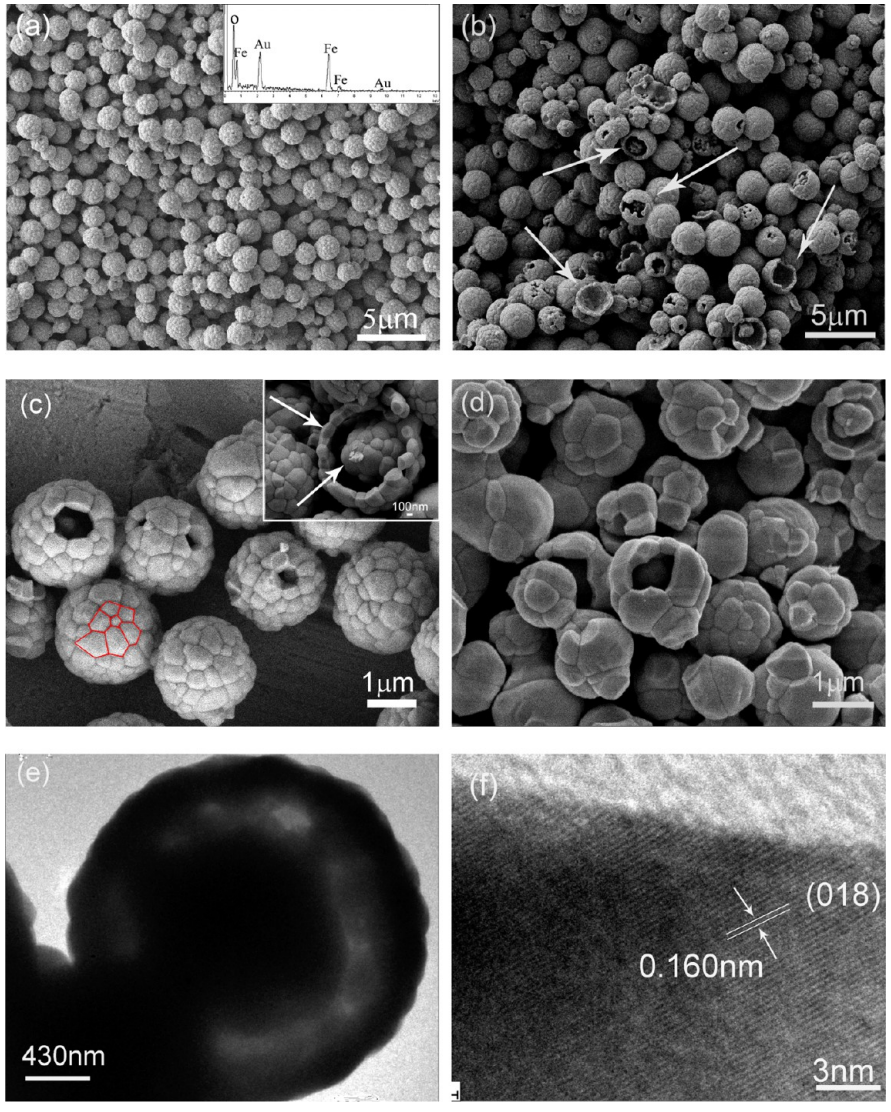


**Figure 4.** (a–c) SEM, (e) TEM, and (f) HRTEM images of the $\alpha$-$Fe_2O_3$ microspheres obtained after 900 °C calcination for 10 min; inset in panel a: EDX analysis; (d) SEM image of the $\alpha$-$Fe_2O_3$ microspheres obtained after 900 °C calcination for 30 min.

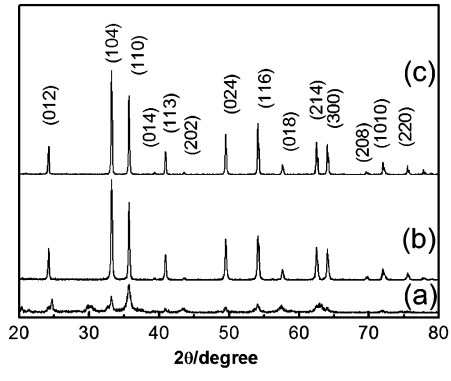


**Figure 5.** XRD patterns of the products calcined for 24 h at (a) 500, (b) 600, and (c) 700 °C.

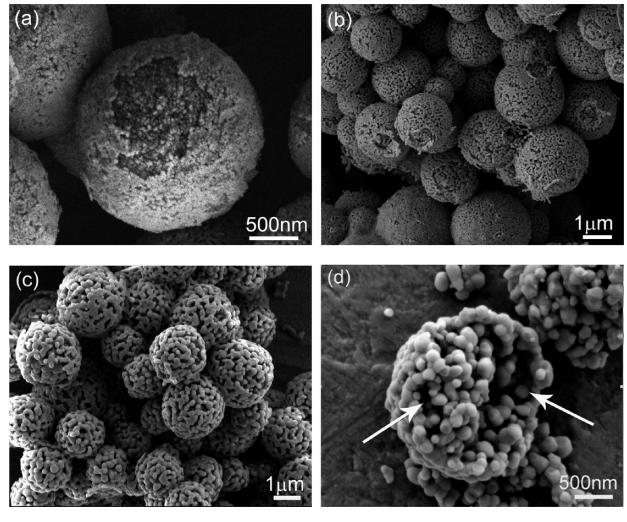


**Figure 6.** SEM images of the products calcined for 24 h at (a) 500, (b) 600, and (c, d) 700 °C.

interplanar spacing of (018) of hematite. However, when the calcination time is prolonged to 30 min, further fusion between the quasi-pentagon and hexagon patches in the shell occurs, leaving fewer striations, and some microspheres also fuse into together, as shown in Figure 4d. To the best of our knowledge,

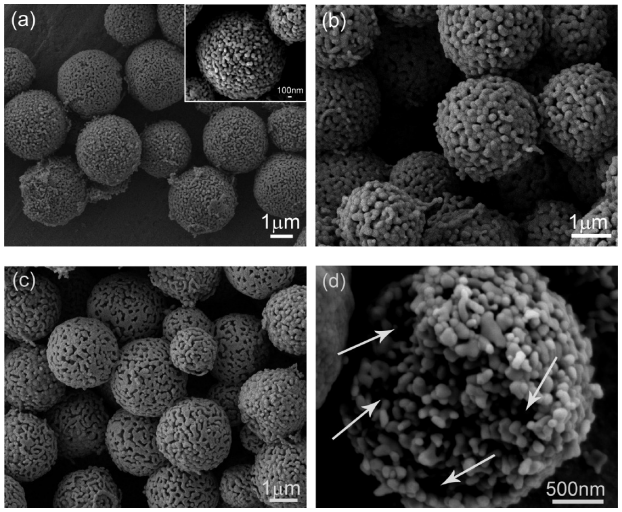


**Figure 7.** SEM images of the products calcined at 700 °C for (a) 1, (b) 4, and (c, d) 12 h.

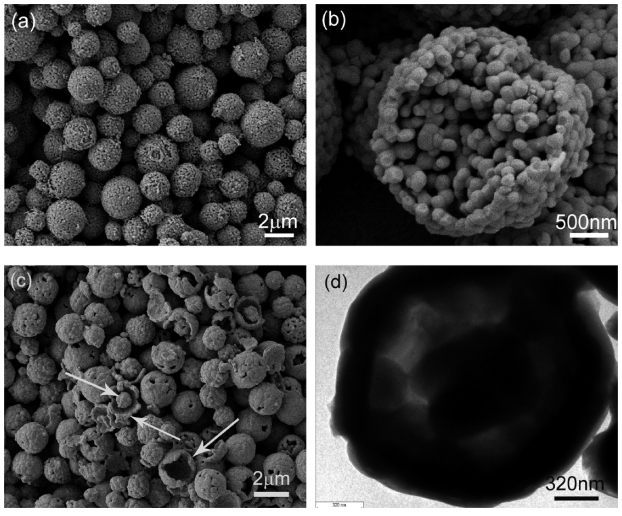


**Figure 8.** (a, b) SEM image of products calcined at 800 °C for 1 h; (c) SEM and (d) TEM images of products calcined at 800 °C for 4 h.

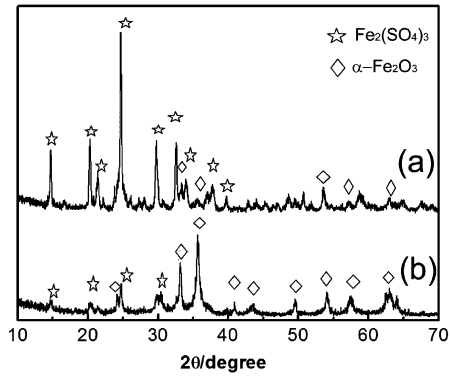


**Figure 9.** XRD patterns of the products calcined at (a) 400 °C for 24 h and (b) 500 °C for 12 h.

this is the first report on the synthesis of homogeneous hollow core/shell hematite microspheres by calcination of the pyrite-PVP microspheres.

It has be found that the final phases obtained by the transformation of pyrite in an oxygen-containing atmosphere

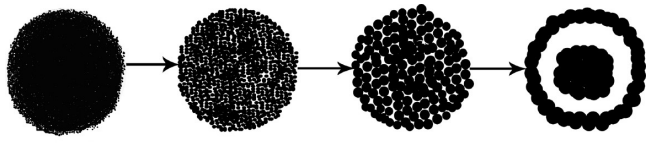

**Figure 10.** Schematic illustration for the formation of hollow core/shell hematite microspheres.

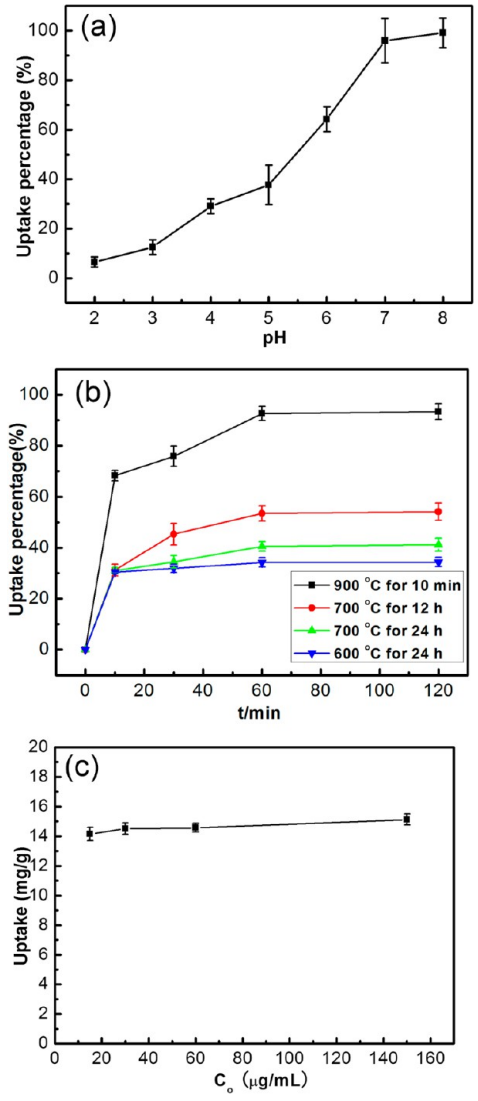


**Figure 11.** (a) Effect of pH on the removal of samarium(III) ions by the hollow core/shell hematite microspheres obtained at 900 °C for 10 min; (b) effect of contact time on the removal of samarium(III) ions at pH 7.0 by the typical hematite microspheres prepared under different calcination conditions; (c) effect of initial concentrations of Sm (III) on the removal of Sm (III) at pH 7.0 by the hollow core/shell hematite microspheres.

can be affected by parameters such as temperature, particle size, flow condition, and properties of the surrounding atmosphere.[42] Therefore, the calcination experiments with different temperatures were also carried out. The XRD patterns of the calcined products obtained at 500, 600, and 700 °C for 24 h are shown in Figure 5, respectively. All of the XRD patterns can be indexed to the pure phase of hematite except that the product obtained at 500 °C exhibits the broaden diffraction peaks,

**Table 1. $Sm^{3+}$ Removal Capacities of Various Adsorbents**

| adsorbent sample | maximum adsorption capacity | ref |
|---|---|---|
| nanoscale zerovalent iron (nZVI) | 10 mg/g | 61 |
| alumina-supported nZVI (Al-nZVI) | 9.49 mg/g | 61 |
| $Al_2O_3$ | 4.6 mg/g | 61 |
| synthetic analogue of heulandite | 0.17 mequiv/g (323 K) | 62 |
| bentonite modified with N-(2-hydroxyethyl) ethylenediamine | 17.7 mg/g | 63 |
| hollow core/shell hematite | 14.48 mg/g | this work |

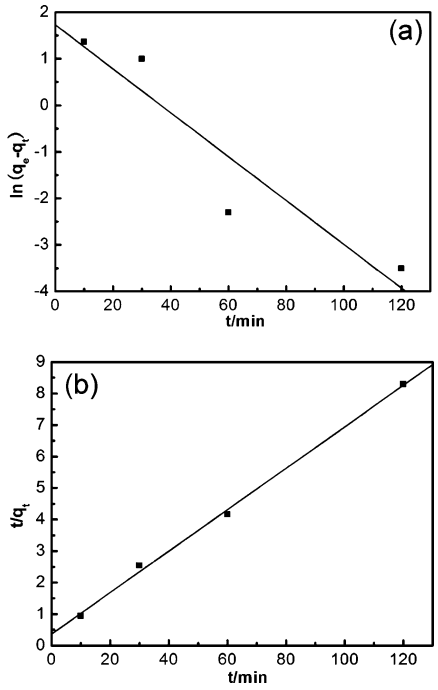


**Figure 12.** (a) Linear first-order kinetic sorption data and (b) pseudo-second kinetic sorption date for Sm(III) by hollow core/shell hematite microspheres.

suggesting that higher temperatures facilitate the crystallization and growth of hematite. Figure 6 depicts the SEM images of the corresponding calcined products. Figure 6a clearly exhibits that the $\alpha$-$Fe_2O_3$ microspheres obtained at 500 °C for 24 h are composed of nanoparticles with ~50 nm, whereas a 600 °C calcination treatment leads to fusion and growth of some small nanoparticles on the surface of microsphere so that a loose net-like surface texture can be observed (Figure 6b). Raising the temperature to 700 °C, it is not difficult to find from Figure 6c that further fusion and growth of the nanoparticles on the microsphere surfaces occur. Moreover, in order to identity the interior structures, the hematite microspheres obtained at 700 °C was first ground for a few seconds, and then observed by SEM. The SEM image of a typical broken microsphere (e.g., Figure 6d) clearly reveals that the interior of the hematite microsphere is almost composed of spherical nanoparticles, no significant aggregation and fusion among the nanoparticles occurs. As a result, the core/shell structures cannot be formed at 700 °C even though 24 h of calcination is performed (Figure 6c, d).

The relative compact surfaces of the hematite microspheres (Figure 6c) and some circular empty spaces inside the microsphere, as highlighted by white arrows in Figure 6d, also reveal that a mass transportation process from the interior to exterior of the microspheres should occur, and such mass transportation is much more rapid with raising the calcination temperature, so that a 10 min of calcination at 900 °C leads to the formation of hematite microspheres with football-like textures (Figure 4). It appears that calcination temperature plays a very important role in controlling the formation of the hollow core/shell hematite microspheres.

To further understand the details in the formation of the hollow core/shell hematite microspheres, we carried out some time-dependent calcination experiments at 700 and 800 °C. Figure 7 shows the SEM results of the $FeS_2$ microspherolites calcined at 700 °C for 1, 4, and 12 h. One can see from Figure 7a that the microspheres consist of nanoparticles with the size ~100 nm after 1 h of calcination. With the calcination time prolonging to 4 h, the exterior nanoparticles become bigger compared with Figure 7a, and the larger particles may be formed by the aggregation and fusion of tiny nanoparticles, leaving a few larger voids, due to the requirement for minimizing the surface energy. When the calcination time reaches to 12 h, the nanoparticles on the surface of the hematite microspheres further fuse one another, forming the net-like textures (Figure 7c). The SEM image (Figure 7d) of a broken microsphere also shows the occurrence of the subunit fusion in the inner structure, as the size of the subunit particles ranges from ~100 to 300 nm, and the circular empty spaces inside the microsphere can be distinctly visualized (as indicated by arrows). When the pyrite precursors is calcined at 800 °C for 1 h, the calcined product exhibits similar texture characteristics to that obtained at 700 °C for 4 h, as shown in Figure 8a. And the close-up image of a broken microsphere further reveals that the hematite microspheres are composed of submicrometer particles (Figure 8b). However, hematite with hollow core/shell structure is obtained when the pyrite microspherolites are heated at 800 °C for 4 h, as certified by the SEM and TEM observations (Figure 8c and d), and the calcined product nearly has similar morphology and architecture characteristics to the typical product obtained at 900 °C for 10 min (e.g., Figure 4).

It can be safely concluded from the temperature- and time-dependent experiments that the calcination temperature is a crucial factor in the formation of the hollow core/shell structures. The hollow core/shell microspheres cannot be formed at temperatures below 800 °C even though a 24 h of calcination is completed (e.g., Figure 6d). However, the hollow core/shell structures can be obtained through a 4 h of calcination at 800 °C (Figure 8c, d), and only 10 min at 900 °C (Figure 4). In other words, the formation time of the specific

**Table 2. Kinetic Parameters for the Adsorption of $Sm^{3+}$ onto Hollow Core/Shell Hematite Microspheres Based on the First-Order and Pseudo-Second-Order Kinetic Models**

| experimental parameters | | pseudo-first order | | | pseudo-second order | | |
|---|---|---|---|---|---|---|---|
| pH | $q_{e,exp}$ (mg/g) | $k_1$ ($min^{-1}$) | $q_{e,cal}$ (mg/g) | $R^2$ | $k_2$ (g/mg min) | $q_{e,cal}$ (mg/g) | $R^2$ |
| 7 | 14.48 | 0.047 | 5.63 | 0.880 | 86.63 | 15.38 | 0.997 |

hollow core/shell structures can be considerably shortened at a high calcining temperature. Moreover, the crystal aggregation and fusion, and the mass transport are the essential processes in the formation of the hollow core/shell hematite.

In an oxygen-containing atmosphere, pyrite can be oxidized to hematite directly or after it is decomposed to pyrrhotite $FeS_x$ (here $1 \leq x \leq 2$).[42] This is determined by the relative rates between the oxygen diffusion to the pyrite core and the thermal decomposition of the pyrite, and hence depends on the actual conditions, such as temperature, oxygen concentration and flow, as well as particle size. The direct oxidation of pyrite normally takes place at temperatures lower than about 527 °C and at higher oxygen concentrations, whereas the two-step process normally takes place under opposite conditions. Moreover, sulfates (mainly ferrous sulfate and ferric sulfate) can be formed as minor product in the oxidation process of pyrite/pyrrhotite.[43,49,50] The formation of sulfates is probably determined by the gas composition at the reaction front. Ferrous sulfate usually forms in a gas that is rich in $SO_2$, whereas ferric sulfate in a gas enriched in $SO_3$.[42] In our case, the pyrite-PVP precursor was also calcined at 400 °C for 24 h and 500 °C for 12 h to understand the chemical reaction details from pyrite to hematite. XRD analyses show that $Fe_2(SO_4)_3$ is the main phase (JCPDS card No.73−0573; space group $R\bar{3}$) aside from a trace of hematite in the sample treated at 400 °C for 24 h (Figure 9a). In contrast, massive hematite and a small amount of $Fe_2(SO_4)_3$ coexist after 500 °C calcination for 12 h (Figure 9b), further confirming that the arrest of the heating losing weight on the TG curve (Figure 2) originates from the decomposition of $Fe_2(SO_4)_3$. Because no pyrrhotite and ferrous sulfate are identified in our experiments, the main reactions involved in the transformation from pyrite to hematite can be generalized as follows

$$2FeS_2(s) + 5.5O_2(g) \rightarrow Fe_2O_3(s) + 4SO_2(g) \quad (1)$$

$$2FeS_2(s) + 7O_2(g) \rightarrow Fe_2(SO_4)_3(s) + 4SO_2(g) \quad (2)$$

$$Fe_2(SO_4)_3(s) \rightarrow Fe_2O_3(s) + 3SO_3(g) \quad (3)$$

$$SO_3(g) \rightarrow SO_2(g) + 0.5O_2(g) \quad (4)$$

According to the TG-DSC and XRD analyses (Figures 2 and 9), it can be readily identified that reactions 1 and 2 are concomitant with the combustion of the occluded PVP and occur at temperatures of 390−450 °C. As a result, most of the pyrite directly oxidizes into hematite, and only a small amount of pyrite transforms into ferric sulfate. Reactions 3 and 4 occur in the temperature range 450−640 °C, corresponding to the arrest on the TG curve. The temperature at which the reaction begins is determined by the size of pyrite grains, usually bigger grains needs higher temperature, such as 410 °C below 0.074 mm, 440 °C for 0.295−0.417 mm, 460 °C for 1.168−2.362 mm.[49−51] The reaction begins to occur in our experiments at around 390 °C, as shown in the TG-DSC curves (Figure 2), which can be attributed to the smaller size of pyrite particles in the precursor, because the precursor microspherolites constructed of small pyrite nanoparticles should have larger interfacial area available for oxidation, and react at a faster rate.[45]

Moreover, in our case, the oxidation of pyrite may also occur via a shrinking core mechanism, with the increasing movement of the reaction front toward the center of the pyrite particles.[49] Figure 6a shows that porous oxide layers were formed in the inner part of the microspheres, when the pyrite-PVP precursor was calcined at 500 °C for 24 h. This is consistent with the previous report.[42] The appearance of a denser outer layer may be due to the formation of $Fe_2(SO_4)_3$ because the molar volume of $Fe_2(SO_4)_3$ is much higher than those of iron oxides.[42] Once the temperatures surpass 600 °C, the $Fe_2(SO_4)_3$ would be decomposed into hematite (Figure 2), and porous hematite microspherolites are finally formed (Figure 6b, c), meanwhile the combustion of PVP occluded in the precursor also plays a key role in the formation of hollow core/shell texture, which makes the hematite submicrometer-spheres have enough space to restructure. Generally, after a series of transformation reactions 1−4, porous hematite microspheres composed of nanoparticles are formed, and then the smaller nanoparticles aggregate together, forming hematite submicrometer spheres with increasing calcination time. In short, the formation of the core can be ascribed to the aggregation and fusion of the inner hematite submicrometer-spheres, whereas the formation of the densification shell should be attributed to the aggregation and fusion of the external submicrometer-spheres, as well as concomitant mass transportation from the interior to exterior of the hematite microspheres, finally leading to the hollow core/shell architectures, and such process may be driven by minimizing the total energy of the system. A plausible formation mechanism is schematically illustrated in Figure 10.

In recent decades, as the rapid increase in the exploitation of rare earth elements (REEs) resources and its wide application to modern industry and daily life, more and more REEs enter the environment.[52] Moreover, being heavy metals, the REEs from anthropogenic sources usually get into the environment in biologically available forms, and may enter the bodies of human being via food chain and cause adverse health effects. For instance, trivalent ions, such as La (III) and Gd (III), can interfere with calcium channels in human and animal cells, and also alter or even inhibit the action of various enzymes and regulate synaptic transmission, as well as block some receptors (for example, glutamate receptors) when they are found in neurons.[53−55] Therefore, the removal of the REEs entering the environment by human activities will be a continuing concern.

Hematite has been proved as one of the environmental friendly materials, and shown good adsorption performance for heavy metals, such as $Pb^{2+}$, $Cd^{2+}$, $Cr^{3+}$, and so on.[8,31] In this context, the adsorption property of the hollow core/shell hematite microspheres for samarium(III) was tested. The special selection for samarium(III) is because it is a typical member of the lanthanide series, and widely used as neutron absorber in nuclear industry, as a chemical reagent in organic synthesis in chemistry, and most important of all, in radio pharmacy (radioactive samarium-153 is used in medicine to treat the severe pain associated with cancers that have spread to the bones).[56,57]

It is well-known that hematite cannot exist under the low-pH circumstance, and precipitation of $Sm(OH)_3$ (s) would occur at higher pH values. Therefore, the parameter pH is usually believed to be one of the most important factors affecting adsorption process.[58,59] Here, the effect of pH on the adsorption of samarium(III) onto hematite hollow microspheres was studied at pH 2−8, samarium(III) concentration $1 \times 10^{-4}$ mol $L^{-1}$, adsorbent concentration 1.0 g $L^{-1}$, and temperature 298 K. A pH range from 2 to 8 was specially selected, which depends on the concentration of samarium(III) stock solution used ($1 \times 10^{-4}$ mol $L^{-1}$) and the $K_{sp}$ of $Sm(OH)_3$ (s) ($8.2 \times 10^{-23}$ at 25 °C)[60] (Theoretically,

$Sm(OH)_3$ can precipitate out of the stock solution of $1 \times 10^{-4}$ mol $L^{-1}$ when the pH exceeds 7.97). Figure 11a shows the effect of pH on $Sm^{3+}$ removal efficiency by the hollow core/shell hematite microspheres prepared at 900 °C for 10 min. The removal percentage of the samarium ions is found to significantly increase with the initial pH of $Sm^{3+}$ solution and to approach a maximum at pH 7.0, and thereafter it does not change very much with further increase in pH. As is known that the surface charge of adsorbent is neutral at the point of zero charge (PZC), and the adsorbent surface is positively charged below the pHzpc. The pHzpc for hematite is about 8.5.[10] Therefore, the low samarium uptakes at low pH values are most probably due to the protonation of the active sites in hematite, which inhibits their binding ability toward samarium ions. However, as the pH increases, the surface positive charge of hematite decreases, and thus the uptake of samarium ions increases. Therefore, it can be concluded from the results that the adsorption performance of samarium(III) onto hematite is significantly dependent on the initial pH of $Sm^{3+}$ solution, and pH 7.0 was selected in the subsequent sorption experiments in order to avoid the possible precipitation of $Sm^{3+}$ ions. Figure 11b shows the uptake percentage of samarium(III) versus contact time (0−120 min) for the typical hematite microspheres prepared at 600 °C for 24 h (Figure 6b), 700 °C for 12 (Figure 7c, d) and 24 h (Figure 6c, d), and 900 °C for 10 min (Figure 4a−e). It shows a very rapid adsorption of the samarium ions during the first 10 min, subsequently, the adsorption rate decreases gradually and the adsorption contents reach equilibrium after about 60 min for all of the microspheres. Nevertheless, the core/shell hollow hematite microspheres always exhibit the highest uptake percentage than other hematite microspheres. Moreover, the uptake percentage of hematite prepared at 700 °C for 12 h is higher than those prepared at 600 and 700 °C for 24 h, and the hematite prepared at 600 °C for 24 h shows the lowest uptake percentage. The differences in the adsorption performance of the four typical hematite microspheres can be attributed to their different constructed structures (e.g., Figures 4a−e, 6b−d, 7c, d). As a result, the hematite microspheres obtained under different calcination conditions have different specific surface areas. The BET analyses show that the hollow core/shell microspheres indeed have higher specific surface area (5.055 $m^2/g$) than the microspheres prepared at 700 °C for 12 h (3.756 $m^2/g$). In addition, the effect of $Sm^{3+}$ concentration-dependence on the capacity of the hematite hollow core/shell microspheres was also investigated. As shown in Figure 11c, while the dosage of the adsorbent remains constant (1.0 g/L), the uptake amount of samarium ions nearly shows no changes with the increase in initial metal ion concentration. This implies that the adsorption capacity of the core/shell hollow microspheres has reached to saturation at the initial samarium concentration of 15 mg/L, and the maximum adsorption capacity of the hollow microspheres is found to be ca.14.48 mg/g for Sm (III) at pH 7.0. This value is higher than those of previously reported materials, such as nanozero valent iron (nZVI),[61] alumina-supported nZVI (Al-nZVI),[61] $Al_2O_3$,[61] synthetic analogue of heulandites,[62] and is close to that of bentonite modified with N-(2-hydroxyethyl),[63] as summarized in Table 1. These results indicate that the hollow core/shell hematite microspheres have a large adsorption capacity for Sm (III) and can be potentially applied to the removal of other REEs in the water environment.

In order to further understand the adsorption kinetics of the hollow core/shell hematite microspheres, the batch experimental results were fitted with first-order and pseudo-second-order models, respectively. The Lagergren first-order and pseudo-second-order rate equations are as follows[64,65]

$$\ln(q_e - q_t) = \ln q_e - k_1 t \text{ (Lagergren first-order rate equation)}$$

$$t/q_t = 1/k_2 q_e^{\,2} + t/q_e \text{ (pseudo-second-order rate equation)}$$

where $q_e$ and $q_t$ are the amount of adsorbate adsorbed (mg/g) at equilibrium and at any time $t$ (min); $k_1$ and $k_2$ are the adsorption rate constant of first-order or pseudo-second-order adsorption, respectively. If first-order kinetics is applicable, the values of $k_1$ and $q_e$ can be derived from the intercept and slope of the plot of $\ln(q_e - q_t)$ versus $t$, respectively. Similarly, the plot of $t/q$ versus t of pseudo-second-order adsorption should give a linear relationship, from which $q_e$ and $k_2$ can be determined from the slope and intercept of the plot. Figure 12 depicts the linear plots of first-order and pseudo-second-order adsorption for $Sm^{3+}$ ions by the core/shell hollow microspheres, and the kinetic parameters for the adsorption of $Sm^{3+}$ ions onto hollow core/shell hematite microspheres are summarized in Table 2. Figure 12 and the values of the correlation coefficient ($R^2$) listed in Table 2 unambiguously reveal that the kinetics of adsorption for Sm(III) can be explained more accurately by the pseudo-second-order kinetic model.

## CONCLUSIONS

In summary, hematite with hollow core/shell microstructures have been successfully prepared by a simply calcination of PVP-pyrite hybrid microspherolites in air. The formation from the precursor to the hollow core/shell hematite microspheres experiences the oxidation and sulfation of pyrite, combustion of occluded PVP, desulfation, aggregation and fusion of nanosized hematite, as well as mass transportation from the interior to exterior of the microspheres. Calcining temperature plays a crucial factor to control the hollow structure formation, and the combustion of PVP makes the hematite nanoparticles have ample space to restructure. The aggregation of hematite nanocrystals and the core shrinking during the oxidation of pyrite should be responsible for the formation of the hollow structures. The hematite microspheres showed good adsorption ability to remove samarium ions in water treatment and are expected to be useful in removal rare earth elements (REE) and also provide references for dealing with radioactive nuclides, as the samarium has radionuclides such as Sm-149 and Sm-153. This work provides a new method to synthesize metal oxides with controlled morphologies and complex architectures. Because of the unique 3D structure of hollow core/shell hematite microspheres, this kind of novel superstructure can be also expected to have potential applications in catalysis, catalyst support, magnetic devices, drug delivery, and other fields.

## AUTHOR INFORMATION

### Corresponding Author

*E-mail: gtzhou@ustc.edu.cn. Tel.: 86 551 63600533. Fax: 86 551 63600533.

### Notes

The authors declare no competing financial interest.

## ■ ACKNOWLEDGMENTS

This work was partially supported by the Chinese Ministry of Science and Technology (2014CB846003), the Natural Science Foundation of China (41272054), and the Specialized Research Fund for the Doctoral Program of Higher Education (20133402130007).

## ■ REFERENCES

(1) Cornell, R. M.; Schwertmann, U. *The Iron Oxides: Structure, Properties, Reactions, Occurrence and Uses*, 1st ed.; VCH Verlagsgesellschaft: Weinheim, Germany, 1996.

(2) Xu, J. S.; Zhu, Y. J. $\alpha$-$Fe_2O_3$ Hierarchically Nanostructured Mesoporous Microspheres: Surfactant-Free Solvothermal Combined with Heat Treatment Synthesis, Photocatalytic Activity and Magnetic Property. *CrystEngComm* **2012**, *14*, 2702−2710.

(3) Wu, C. Z.; Yin, P.; Zhu, X.; OuYang, C. Z.; Xie, Y. Synthesis of Hematite ($\alpha$-$Fe_2O_3$) Nanorods: Diameter-Size and Shape Effects on Their Applications in Magnetism, Lithium Ion Battery, and Gas Sensors. *J. Phys. Chem. B* **2006**, *110*, 17806−17812.

(4) Mao, D.; Yao, J. X.; Lai, X. Y.; Yang, M.; Du, J.; Wang, D. Hierarchically Mesoporous Hematite Microspheres and their Enhanced Formaldehyde-Sensing Properties. *Small* **2011**, *7*, 578−582.

(5) Jordan, A.; Scholz, R.; Maier-Hauff, K.; Johannsen, M.; Wust, P.; Nadobny, J.; Schirra, H.; Schmidt, H.; Deger, S.; Loening, S.; Lanksch, W.; Felix, R. Presentation of a New Magnetic Field Therapy System for the Treatment of Human Solid Tumors with Magnetic Fluid Hyperthermia. *J. Magn. Magn. Mater.* **2001**, *225*, 118−126.

(6) Zeng, H.; Li, J.; Liu, J. P.; Wang, Z. L.; Sun, S. H. Exchange-Coupled Nanocomposite Magnets by Nanoparticles Self-Assembly. *Nature* **2002**, *420*, 395−398.

(7) Chen, J.; Xu, L. N.; Li, W. Y.; Gou, X. L. $\alpha$-$Fe_2O_3$ Nanotubes in Gas Sensor and Lithium-Ion Battery Applications. *Adv. Mater.* **2005**, *17*, 582−586.

(8) Zeng, S. Y.; Tang, K. B.; Li, T. W.; Liang, Z. H.; Wang, D.; Wang, Y. K.; Zhou, W. W. Hematite Hollow Spindles and Microspheres: Selective Synthesis, Growth Mechanisms, and Application in Lithium Ion Battery and Water Treatment. *J. Phys. Chem. C* **2007**, *111*, 10217−10225.

(9) Ruttenberg, K. C.; Sulak, D. J. Sorption and Desorption of Dissolved Organic Phosphorus onto Iron (oxyhydr)oxides in Seawater. *Geochim. Cosmochim. Acta* **2011**, *75*, 4095−4112.

(10) Pochard, I.; Denoyel, R.; Couchot, P.; Foissy, A. Adsorption of Barium and Calcium Chloride onto Negatively Charged $\alpha$-$Fe_2O_3$ Particles. *J. Colloid Interface Sci.* **2002**, *255*, 27−35.

(11) Wu, R. C.; Qu, J. H.; Chen, Y. S. Magnetic Powder MnO−$Fe_2O_3$ Composite—a Novel Material for the Removal of Azo-Dye from Water. *Water Res.* **2005**, *39*, 630−638.

(12) Hu, J. S.; Zhong, L. S.; Song, W. G.; Wan, L. J. Synthesis of Hierarchically Structured Metal Oxides and their Application in Heavy Metal Ion Removal. *Adv. Mater.* **2008**, *20*, 2977−2982.

(13) Bronstein, L. M.; Huang, X. L.; Retrum, J.; Schmucker, A.; Pink, M.; Stein, B. D.; Dragnea, B. Influence of Iron Oleate Complex Structure on Iron Oxide Nanoparticle Formation. *Chem. Mater.* **2007**, *19*, 3624−3632.

(14) Chueh, Y. L.; Lai, M. W.; Liang, J. Q.; Chou, L. J.; Wang, Z. L. Systematic Study of the Growth of Aligned Arrays of $\alpha$-$Fe_2O_3$ and $Fe_3O_4$ Nanowires by a Vapor−Solid Process. *Adv. Funct. Mater.* **2006**, *16*, 2243−2251.

(15) Zhao, Y. M.; Li, Y. H.; Ma, R. Z.; Roe, M. J.; Mccartney, D. G.; Zhu, Y. Q. Growth and Characterization of Iron Oxide Nanorods/Nanobelts Prepared by a Simple Iron−Water Reaction. *Small* **2006**, *2*, 422−427.

(16) Jia, C. J.; Sun, L. D.; Yan, Z. G.; You, L. P.; Luo, F.; Han, X. D.; Pang, Y. C.; Zhang, Z.; Yan, C. H. Single-Crystalline Iron Oxide Nanotubes. *Angew. Chem., Int. Ed.* **2005**, *44*, 4328−4333.

(17) Ni, Y. H.; Ge, X. W.; Zhang, Z. C.; Ye, Q. Fabrication and Characterization of the Plate-Shaped $\gamma$-$Fe_2O_3$ Nanocrystals. *Chem. Mater.* **2002**, *14*, 1048−1052.

(18) Chin, K. C.; Chong, G. L.; Poh, C. K.; Van, L. H.; Sow, C. H.; Lin, J. Y.; Wee, A. T. S. Large-Scale Synthesis of $Fe_3O_4$ Nanosheets at Low Temperature. *J. Phys. Chem. C* **2007**, *111*, 9136−9141.

(19) Gou, X. L.; Wang, G. X.; Park, J. S.; Liu, H.; Yang, J. Monodisperse Hematite Porous Nanospheres: Synthesis, Characterization, and Applications for Gas Sensors. *Nanotechnology* **2008**, *19*, 125606−125612.

(20) Zhu, L. P.; Xiao, H. M.; Liu, X. M.; Fu, S. Y. Template-Free Synthesis and Characterization of Novel 3D Urchin-Like $\alpha$-$Fe_2O_3$ Superstructures. *J. Mater. Chem.* **2006**, *16*, 1794−1797.

(21) Jung, Y. S.; Son, Y. H.; Lee, J. K. 3-D Self-assembly of Flower-Like Particles via Microwave Irradiation for Water Treatment. *RSC Adv.* **2012**, *2*, 5877−5884.

(22) Hou, Y.; Zuo, F.; Dagg, A.; Feng, P. Y. Visible Light-Driven $\alpha$-$Fe_2O_3$ Nanorod/Graphene/$BiV_{1-x}Mo_xO_4$ Core/Shell Heterojunction Array for Efficient Photoelectrochemical Water Splitting. *Nano Lett.* **2012**, *12*, 6464−6473.

(23) Kanie, K.; Muramatsu, A. Organic-Inorganic Hybrid Liquid Crystals: Thermotropic Mesophases Formed by Hybridization of Liquid-Crystalline Phosphates and Monodispersed $\alpha$-$Fe_2O_3$ Particles. *J. Am. Chem. Soc.* **2005**, *127*, 11578−11579.

(24) Song, H. J.; Jia, X. H.; Li, N.; Yang, X. F.; Tang, H. The Electrochemical Flow Capacitor: a New Concept for Rapid Energy Storage and Recovery. *J. Mater. Chem.* **2012**, *22*, 895−902.

(25) Fei, J. B.; Cui, Y.; Zhao, J.; Gao, L.; Yang, Y.; Li, J. B. Large-Scale Preparation of 3D Self-assembled Iron Hydroxide and Oxide Hierarchical Nanostructures and their Applications for Water Treatment. *J. Mater. Chem.* **2011**, *21*, 11742−11746.

(26) Wei, Z. H.; Xing, R.; Zhang, X.; Liu, S.; Yu, H. H.; Li, P. C. Facile Template-Free Fabrication of Hollow Nestlike $\alpha$−$Fe_2O_3$ Nanostructures for Water Treatment. *ACS Appl. Mater. Interfaces* **2013**, *5*, 598−604.

(27) Woo, K.; Lee, H. J.; Ahn, J. P.; Park, Y. S. Sol-Gel Mediated Synthesis of $Fe_2O_3$ Nanorods. *Adv. Mater.* **2003**, *15*, 1761−1764.

(28) Wu, Z. C.; Yu, K.; Zhang, S. D.; Xie, Y. Hematite Hollow Spheres with a Mesoporous Shell: Controlled Synthesis and Applications in Gas Sensor and Lithium Ion Batteries. *J. Phys. Chem. C* **2008**, *112*, 11307−11313.

(29) Jia, X. H.; Song, H. J. Facile Synthesis of Monodispersed $\alpha$-$Fe_2O_3$ Microspheres through Template-Free Hydrothermal Route. *J. Nanopart. Res.* **2012**, *14*, 663−670.

(30) Yu, J. G.; Yu, X. X.; Huang, B. B.; Zhang, X. Y.; Dai, Y. Hydrothermal Synthesis and Visible-Light Photocatalytic Activity of Novel Cage-Like Ferric Oxide Hollow Spheres. *Cryst. Growth Des.* **2009**, *9*, 1474−1480.

(31) Zhong, L. S.; Hu, J. S.; Liang, H. P.; Cao, A. M.; Song, W. G.; Wan, L. J. Self-Assembled 3D Flowerlike Iron Oxide Nanostructures and their Application in Water Treatment. *Adv. Mater.* **2006**, *18*, 2426−2431.

(32) Cao, S. W.; Zhu, Y. J. Hierarchically Nanostructured $\alpha$-$Fe_2O_3$ Hollow Spheres: Preparation, Growth Mechanism, Photocatalytic Property, and Application in Water Treatment. *J. Phys. Chem. C* **2008**, *112*, 6253−6257.

(33) Cheng, X. L.; Jiang, J. S.; Hu, M.; Mao, G. Y.; Liu, Z. W.; Zeng, Y.; Zhang, Q. H. Liquid−Liquid Interface-Assisted Solvothermal Synthesis of Durian-Like $\alpha$-$Fe_2O_3$ Hollow Spheres Constructed by Nano-Polyhedrons. *CrystEngComm* **2012**, *14*, 3056−3062.

(34) Chen, X. Y.; Wang, Z. H.; Wang, X.; Wan, J. X.; Liu, J. W.; Qian, Y. T. Single-Source Approach to Cubic $FeS_2$ Crystallites and their Optical and Electrochemical Properties. *Inorg. Chem.* **2005**, *44*, 951−954.

(35) Wadia, C.; Wu, Y.; Gul, S.; Volkman, S. K.; Guo, J. H.; Alivisatos, A. Surfactant-Assisted Hydrothermal Synthesis of Single Phase Pyrite $FeS_2$ Nanocrystals. *Chem. Mater.* **2009**, *21*, 2568−2570.

(36) Ennaoui, A.; Fiechter, S.; Pettenkofer, Ch.; Alonso-Vante, N.; Buker, K.; Bronold, M.; Hopfner, Ch.; Tributsh, H. Iron Disulfide for Solar Energy Conversion. *Sol. Energy Mater. Sol. Cell* **1993**, *29*, 289−370.

(37) Montoro, L. A.; Rosolen, J. M. Gelatin/DMSO: a New Approach to Enhancing the Performance of a Pyrite Electrode in a Lithium Battery. *Solid State Ionics* **2003**, *159*, 233−240.
(38) Lalvani, S. B.; Shami, M. Electrochemical Oxidation of Pyrite Slurries. *J. Electrochem. Soc.* **1986**, *133*, 1364−1368.
(39) Gao, P.; Xie, Y.; Ye, L. N.; Chen, Y.; Guo, Q. X. From 2D Nanoflats to 2D Nanowire Networks: a Novel Hyposulfite Self-Decomposition Route to Semiconductor $FeS_2$ Nanowebs. *Cryst. Growth Des.* **2006**, *6*, 583−587.
(40) Barnard, A. S.; Russo, S. P. Modelling Nanoscale $FeS_2$ Formation in Sulfur Rich Conditions. *J. Mater. Chem.* **2009**, *19*, 3389−3394.
(41) Kar, S.; Chaudhuri, S. Solvothermal Synthesis of Nanocrystalline $FeS_2$ with Different Morphologies. *Chem. Phys. Lett.* **2004**, *398*, 22−26.
(42) Hu, G. L.; Dam-Johansen, K.; Stig, W.; Hansen, J. P. Decomposition and Oxidation of Pyrite. *Prog. Energy Combust. Sci.* **2006**, *32*, 295−314.
(43) Jorgensen, F. R. A.; Moyle, F. J. Phases Formed during the Thermal Analysis of Pyrite in Air. *J. Therm. Anal.* **1982**, *25*, 473−485.
(44) Li, M. L.; Yao, Q. Z.; Zhou, G. T.; Qu, X. F.; Mu, C. F.; Fu, S. Q. Microwave-Assisted Controlled Synthesis of Monodisperse Pyrite Microspherolites. *CrystEngComm* **2011**, *13*, 5936−5942.
(45) Almeida, C. M. V. B.; Giannetti, B. F. Comparative Study of Electrochemical and Thermal Oxidation of Pyrite. *J. Solid State Electrochem.* **2002**, *6*, 111−118.
(46) Ennaoui, A.; Fietcher, S.; Jaegermann, W.; Tributsch, H. Photoelectrochemistry of Highly Quantum Efficient Single-Crystalline n-$FeS_2$ (Pyrite). *J. Electrochem. Soc.* **1986**, *133*, 97−106.
(47) Jorgensen, F. R. A.; Moyle, F. J. Periodic Thermal Instability during the Isothermal Oxidation of Pyrite. *Metall. Mater. Trans. B* **1981**, *12*, 769−770.
(48) Paulik, F.; Paulik, J.; Arnold, M. Gas Diffusion during the Thermal Analysis of Pyrite. *J. Therm. Anal.* **1986**, *31*, 145−156.
(49) Dunn, J. G.; De, G. C.; O'Connor, B. H. The Effect of Experimental Variables on the Mechanism of the Oxidation of Pyrite: Part 1. Oxidation of Particles Less Than 45 $\mu$m in Size. *Thermochim. Acta* **1989**, *145*, 115−130.
(50) Dunn, J. G.; De, G. C.; O'Connor, B. H. The Effect of Experimental Variables on the Mechanism of the Oxidation of Pyrite: Part 2. Oxidation of Particles of Size 90−125 $\mu$m. *Thermochim. Acta* **1989**, *155*, 135−149.
(51) Clemént, D. *Inorganic Thermogravimetric Analysis*, 2nd ed; Elsevier: New York, 1963.
(52) Ali, O. I. M.; Osman, H. H.; Sayed, S. A.; Shalabi, M. E. H. The Removal of Some Rare Earth Elements from their Aqueous Solutions on By-Pass Cement Dust (BCD). *J. Hazard. Mater.* **2011**, *195*, 62−67.
(53) Hirano, S.; Suzuki, K. T. Exposure, Metabolism, and Toxicity of Rare Earths and Related Compounds. *Environ. Health Perspect.* **1996**, *104*, 85−95.
(54) Chen, Z. Y.; Zhu, X. Z. Accumulation of Rare Earth Elements in Bone and Its Toxicity and Potential Hazard to Health. *J. Ecol. Rural Environ.* **2008**, *24*, 88−91.
(55) Pałasz, A.; Czekaj, P. Toxicological and Cytophysiological Aspects of Lanthanides Action. *Acta Biochim Polym.* **2000**, *47*, 1107−1114.
(56) Anderson, P. M.; Wiseman, G. A.; Dispenzieri, A.; Arndt, C. A. S.; Hartmann, L. C.; Smithson, W. A.; Mullan, B. P.; Bruland, O. S. High-Dose Samarium-153 Ethylene Diamine Tetramethylene Phosphonate: Low Toxicity of Skeletal Irradiation in Patients With Osteosarcoma and Bone Metastases. *J. Clin. Oncol.* **2002**, *20*, 189−196.
(57) Shirvani-Arani, S.; Ahmadi, S. J.; Bahrami-Samani, A.; Ghannadi-Maragheh, M. Synthesis of Nano-Pore Samarium (III)-Imprinted Polymer for Preconcentrative Separation of Samarium Ions from other Lanthanide Ions via Solid Phase Extraction. *Anal. Chim. Acta* **2008**, *623*, 82−88.
(58) Chen, C.; Wang, X. Sorption of Th(IV) to Silica as a Function of pH, Humic/Fulvicacid, Ionic Strength, Electrolyte Type. *Appl. Radiat. Isot.* **2007**, *65*, 155−163.
(59) Ghaemi, A.; Torab-Mostaedi, M.; Ghannadi-Maragheh, M. Characterizations of Strontium(II) and Barium(II) Adsorption from Aqueous Solutions Using Dolomite Powder. *J. Hazard. Mater.* **2011**, *190*, 916−921.
(60) Sun, Y.; Zheng, W. J. Ultrathin $SmVO_4$ Nanosheets: Ionic Liquid-Assisted Hydrothermal Synthesis, Characterization, Formation Mechanism and Optical Property. *Dalton Trans.* **2010**, *39*, 7098−7103.
(61) Yesiller, S. U.; Eroğlu, A. E.; Shahwan, T. Removal of Aqueous Rare Earth Elements (REEs) Using Nano-Iron Based Materials. *J. Ind. Eng. Chem.* **2013**, *19*, 898−907.
(62) Sharma, P.; Singh, G.; Tomar, R. Synthesis and Characterization of an Analogue of Heulandite: Sorption Applications for Thorium(IV), Europium(III), Samarium(II) and Iron(III) Recovery from Aqueous Waste. *J. Colloid Interface Sci.* **2009**, *332*, 298−308.
(63) Li, D. D.; Chang, X. J.; Hu, Z.; Wang, Q. H.; Li, R. J.; Chai, X. L. Samarium (III) Adsorption on Bentonite Modified with N-(2-hydroxyethyl) Ethylenediamine. *Talanta* **2011**, *83*, 1742−1747.
(64) Lagergren, S. Zur theorie der sogenannten adsorption gelöster stoffe. *K. Sven. Vetenskapsakad. Handl.* **1898**, *24*, 1−39.
(65) Ho, Y. S.; McKay, G. Pseoudo-second-order model for sorption processes. *Process Biochem.* **1999**, *34*, 451−465.